Supplementary Information for

Direct Detection of Spin Polarisation in Photoinduced Charge Transfer through a Chiral Bridge

Alberto Privitera[a,b], Emilio Macaluso[c,d], Alessandro Chiesa[c,d], Alessio Gabbani[e], Davide Faccio[f], Demetra Giuri[f], Matteo Briganti[b], Niccolò Giaconi[b,g], Fabio Santanni[b], Nabila Jarmouni[e], Lorenzo Poggini[h], Matteo Mannini[b], Mario Chiesa[a], Claudia Tomasini[f], Francesco Pineider[e], Enrico Salvadori[a], Stefano Carretta[c,d*], Roberta Sessoli[b*]*

[a.] *Department of Chemistry and NIS Centre, University of Torino, Via Giuria 7, I-10125, Torino, Italy*

[b.] *Department of Chemistry "U. Schiff" (DICUS), University of Florence, & UdR INSTM Firenze, Via della Lastruccia 3-13, I-50019, Sesto Fiorentino, Italy*

[c.] *Department of Mathematical, Physical and Computer Sciences, University of Parma, I-43124, Parma, Italy & UdR INSTM Parma*

[d.] *INFN–Sezione di Milano-Bicocca, gruppo collegato di Parma, I-43124 Parma, Italy.*

[e.] *Department of Chemistry and Industrial Chemistry, University of Pisa, & UdR INSTM Pisa, Via Moruzzi 13, I-56124, Pisa, Italy*

[f.] *Department of Chemistry "Giacomo Ciamician", University of Bologna, Via Selmi 2, I-40126, Bologna, Italy*

[g.] *Department of Industrial Engineering (DIEF), University of Florence, & UdR INSTM Firenze, Via Santa Marta 3, I-50139, Firenze, Italy*

[h.] *CNR-ICCOM, Via Madonna del Piano 10, I-50019, Sesto Fiorentino, Italy*

Table of contents

DFT calculations

All DFT calculations have been performed with ORCA 4.2.1 quantum chemistry package.[1] For the geometry optimizations, PBE0 functional[2] and D3 empirical dispersion correction[3-4] were used, while def2-TZVP basis set[5] was employed for all the atoms. The thresholds on the maximum force gradient and the energy change were set to $3 \cdot 10^{-4}$ Hartree/Bohr and to $5 \cdot 10^{-6}$ Hartrees, respectively. The root mean square deviation was computed on the heavy atoms C, N, O, and S of the polypeptide chain within the formula $RMSD = \sqrt{\frac{1}{N}\sum_{i=1}^{N} d_i^2}$ where d_i is the distance between a pair of equivalent atoms in the two structures and N is the total number of equivalent atoms. The optimized structure of **1** and the X-ray structure of the S-protected oligopeptide [Tri-S-$(CH_2)_2$-(CO)-(L-Ala-D-Oxd)$_2$-OBn are shown in Figure S1.
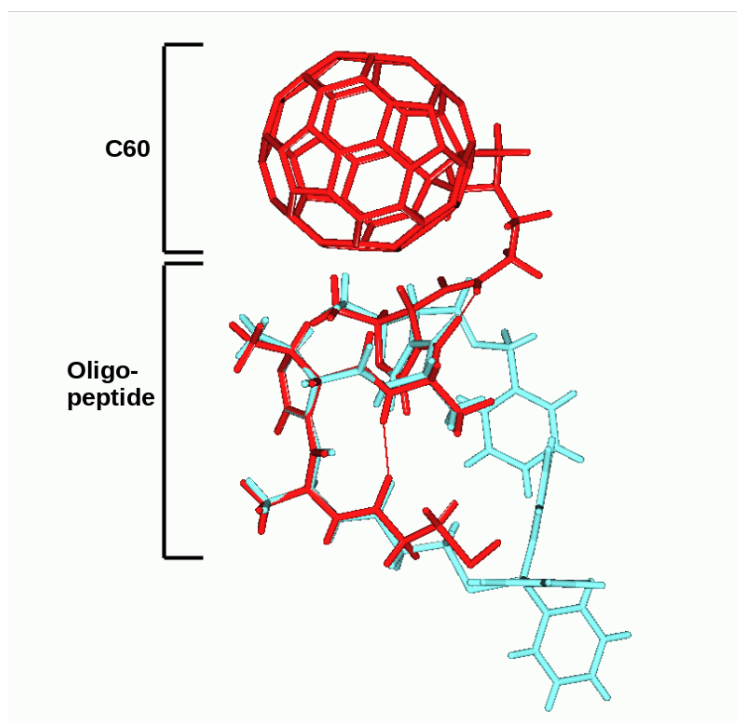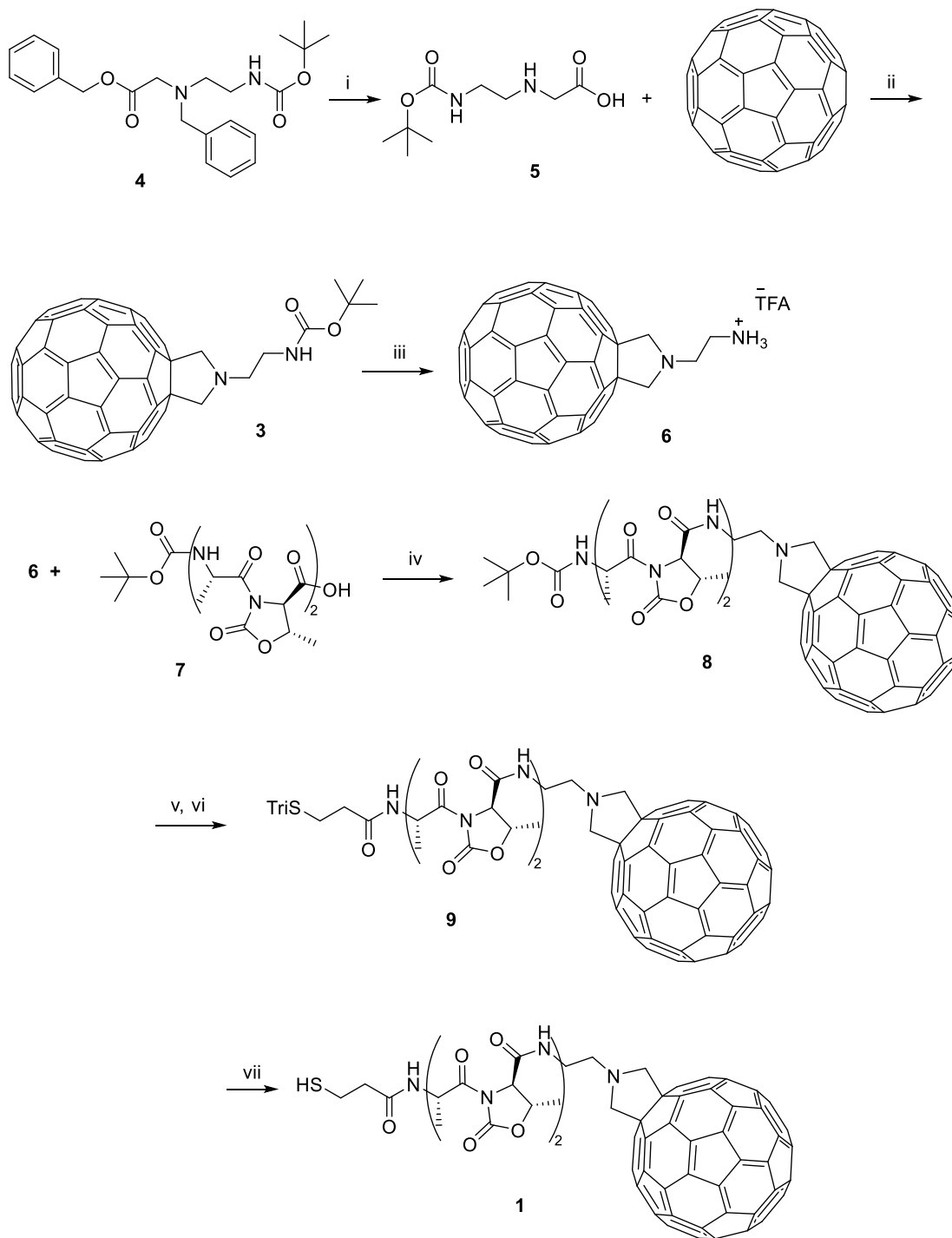

Figure S1. Superimposed structures of the optimized geometry of **1** (red) and the x-ray structure of the S-protected oligopeptide lacking fullerene unit (azure blue).

Synthesis of organic ligands 1, 2 and 3

Scheme S1. Reagents and Conditions: (i) H_2, Pd/C, MeOH, r.t., 4 h, >99% yield; (ii) paraformaldehyde (5 equiv.), toluene, reflux, 1 h, 40% yield; (iii) TFA (200 equiv.), dry CH_2Cl_2, r.t., 4 h, >99% yield; (iv) HBTU (2 equiv.), DIEA (2.2 equiv. + some more to remove possible exceeding

TFA from the previous reaction), dry CH₂Cl₂, r.t., 24 h, 40% yield; (v) TFA (25 equiv.), CH₂Cl₂, r.t., 6 h, 99% yield; (vi) 3-(tritylthio)propanoic acid (1.6 equiv.), HBTU (1.8 equiv.), DIEA (2.2 equiv. + some more to remove possible exceeding TFA from the previous reaction), dry CH₂Cl₂, r.t., 24 h, 56% yield; (vi) Et₃SiH (3.8 equiv.) BF₃.Et₂O (0.2 equiv.), HFIP, r.t., 45 min, 60% yield.
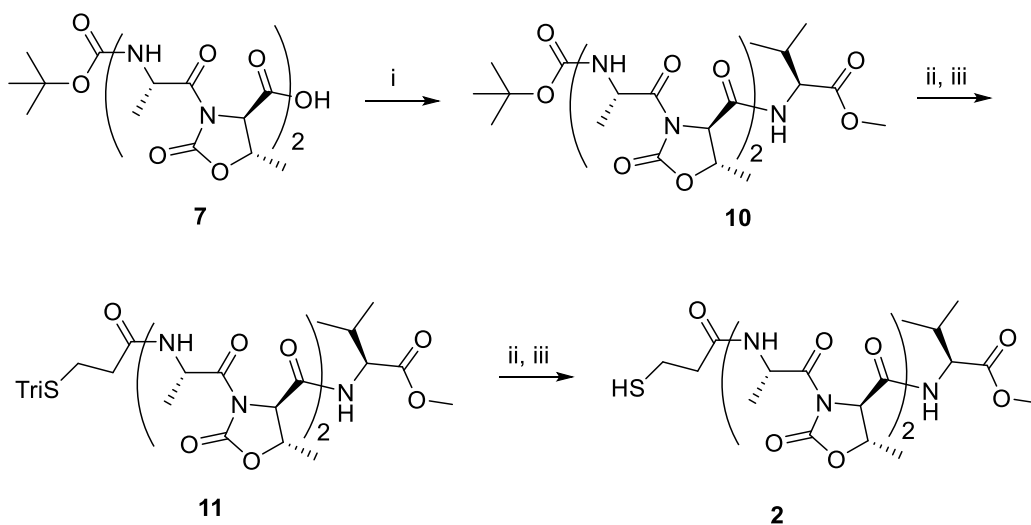
Scheme S2. Reagents and Conditions: (i) L-Val-OMe•HCl (1 equiv.), HBTU (1.1 equiv.), DIEA (3.3 equiv.), dry acetonitrile, r.t., 5 h, 90% yield; (ii) TFA (18 equiv.), CH₂Cl₂, r.t., 6 h, 99% yield; (iii) 3-(tritylthio)propanoic acid (1 equiv.), HBTU (1.1 equiv.), DIEA (2.2 equiv. + some more to remove possible exceeding TFA from the previous reaction), dry acetonitrile, r.t., 24 h, 92% yield; (iv) Et₃SiH (3.8 equiv.) BF₃.Et₂O (0.2 equiv.), HFIP, r.t., 45 min, 75% yield.

All reactions were carried out in dried glassware and using dry solvents. The melting points of the compounds were determined in open capillaries and are uncorrected. High-quality infrared spectra (64 scans) were obtained at 2 cm^{-1} resolution with an ATR-IR Bruker (Billerica, US, MA) Alpha System spectrometer. All compounds were dried in vacuo, and all the sample preparations were performed in a nitrogen atmosphere. NMR spectra were recorded with a Varian (Palo Alto, US, CA) Inova 400 spectrometer at 400 MHz (^{1}H NMR) and at 100 MHz (^{13}C NMR). Chemical shifts are reported in δ values relative to the solvent peak. HPLC-MS analysis was carried out with an Agilent 1260 Infinity II liquid chromatography coupled to an electrospray ionization mass spectrometer (LC-ESI-MS), using a Phenomenex Gemini C18 - 3μ - 110 Å column, H_2O/CH_3CN with 0.2% formic acid as acid solvent at 40 °C (positive ion mode, mz = 50-2000, fragmentor 70 V). To record LC-ESI-MS spectra of the C_{60} derivatives, the compounds were dissolved in 4/1 THF/Methanol.

Synthesis of 4 and 5. Benzyl *N*-benzyl-*N*-(2-((*tert*-butoxycarbonyl)amino)ethyl)glycinate **4** was synthesised as reported in literature.[6] The product was then deprotected from the benzyl groups by hydrogenolysis in presence of catalytic Pd/C, and **5** was obtained as a white solid in quantitative yield as reported in literature.[6]

Synthesis of 3. The product was obtained following the Prato reaction in 40% yield after silica chromatography purification.[7] The characterization matched the values reported in reference.

Synthesis of 6. The Boc group was removed from compound **3** by a 4 h reaction with TFA (trifluoroacetic acid) (200 eq.) in CH_2Cl_2, obtaining compound **4** in quantitative yield. The characterization matched the values reported in reference.[7]

Synthesis of 7. Boc-(L-Ala-D-Oxd)$_2$-OH (**7**) was synthesized as reported in literature.[8] The characterization matched the values reported in reference.

Synthesis of 8. Compound **7** (75 mg, 0.146 mmol) was dissolved in dry CH_2Cl_2 (7 mL), then HBTU (2-(1*H*-benzotriazol-1-yl)-1,1,3,3-tetramethyluronium hexafluorophosphate) (63 mg, 0.165 mmol) was added under nitrogen atmosphere and the mixture was stirred at room temperature for 10 minutes. A solution containing **6** (78 mg, 0.097 mmol) and DIEA (98 μL, 0.57 mmol) in dry CH_2Cl_2 (3 mL) was added dropwise to the mixture, and the reaction was stirred for 24 h. The mixture was diluted with H_2O and extracted twice with CH_2Cl_2. The combined organic layers were dried over Na_2SO_4 and the solvent evaporated under vacuum. The crude residue was purified with silica chromatography (99:1 CH_2Cl_2:MeOH as solvent). Product **8** was obtained as a brown solid in 40% yield after solvent removal.

IR (ATR-IR): ν 3310, 2921, 2849, 1779, 1686, 1508 cm^{-1}. ^{1}H-NMR (400MHz, CDCl$_3$): δ 1.40-1.55 (m, 21H, 9H Boc, 2 CH$_3$ Ala, 2 CH$_3$ Oxd), 3.27 (t, 2H, CH$_2$N-pyrrolidine), 3.69-3.80 (m, 2H, C*H$_2$*CH$_2$N-pyrrolidine), 4.45 (m, 4H, CH$_2$ pyrrolidine), 4.47-4.62 (m, 2H, CH α Oxd), 4.70-4.80 (m, 2H, CH α Ala), 5.10 (bs, 1H, NH Boc), 5.17-5.25 (m, 2H, CH β Oxd), 7.19 (1H, NH amide).

Synthesis of 9. Product **8** (65.2 mg, 0.05 mmol) was dissolved in dry CH$_2$Cl$_2$ (2 mL), then TFA (25 equiv., 0.1 mL) was added, and the mixture was stirred for 6 h. When the deprotection was complete, the solvents were removed under reduced pressure and replaced with dry CH$_2$Cl$_2$ (2 mL). In another flask, 3-(tritylthio)propanoic acid (26 mg, 0.075 mmol) and HBTU (32 mg, 0.085 mmol) were dissolved in dry CH$_2$Cl$_2$ (6 mL) under nitrogen atmosphere, and the mixture was stirred at room temperature for 10 minutes. The solution containing deprotected **8** and DIEA (*N,N*-diisopropylethylamine) (0.106 mL, 0.62 mmol) in dry CH$_2$Cl$_2$ (2 mL) was then added dropwise. The mixture was stirred for 24 h, then it was diluted with H$_2$O and extracted three times with CH$_2$Cl$_2$. The combined organic layers were dried over Na$_2$SO$_4$, and the solvent evaporated under vacuum. The crude residue was purified with silica chromatography (99:1 CH$_2$Cl$_2$:MeOH). Product **9** was obtained as a brown solid in 56% yield.

IR (ATR-IR): ν 3205, 2995, 2956, 2916, 2847, 1739, 1697, 1670 cm^{-1}. ^{1}H-NMR (400MHz, CDCl$_3$): δ 1.27-1.55 (m, 12H, CH$_3$-Ala, CH$_3$-Oxd), 2.44-2.56 (m, 2H, *CH$_2$*CH$_2$STrt), 2.77-3.05 (m, 2H, CH$_2$*CH$_2$*STrt), 3.20 (m, 2H, NH CH$_2$*CH$_2$*N Fulleropyrrolidine), 3.68-3.77 (m, 4H, 2 CH-α-Oxd, NH*CH$_2$*CH$_2$N Fulleropyrrolidine), 4.25 (q, 1H, CHα-Ala) 4.34-4.50 (m, 5H, 2 CH$_2$ Fulleropyrrolidine, 1 CHα-Ala), 4.54-4.75 (m, 2H, CHβ-Oxd), 7.13-7.43 (m, 15 H, CH Ph).

Synthesis of 1. Compound **8** (40 mg, 0.028 mmol) was added to a solution of BF$_3$•Et$_2$O (1 μL, 8.4 μmol), Et$_3$SiH (0.017 mL, 0.107 mmol) in hexafluoroisopropanol (HFIP 0.15 M, 0.112 mL), following a procedure reported in the literature.[9] After 45 min under stirring, the reaction was quenched with NaHCO$_3$ and the residue was extracted three times with CH$_2$Cl$_2$. The combined organic layers were dried over Na$_2$SO$_4$ and the solvent was evaporated under vacuum. The crude residue was purified with silica chromatography (98:2 CH$_2$Cl$_2$:MeOH). Product **1** was obtained as a brown solid (yield 60%). IR (ATR-IR): ν 3060, 3022, 2922, 2855, 1782, 1732, 1652, 1595, 1494 cm^{-1}. ^{1}H-NMR (400MHz, CDCl$_3$): δ 1.21-1.7 (m, 13H, CH$_3$-Ala, CH$_3$-Oxd, SH), 2.51 (t, 2H, CH$_2$*CH$_2$*SH), 2.63 (t, 2H, *CH$_2$*CH$_2$SH), 3.25 (m, 2H, NH CH$_2$*CH$_2$*N Fulleropyrrolidine), 3.70-3.74 (2H, NH*CH$_2$*CH$_2$N Fulleropyrrolidine), 3.76-3.83 (m, 2H, CH-α-Oxd), 4.24 (q, 1H, CH-α-Ala),

4.39-4.52 (m, 5H, 2 CH$_2$ Fulleropyrrolidine, 1 CH-α-Ala), 4.56-4.76 (m, 2H, CH-β-Oxd). ^{13}C-NMR (100 MHz, DMSO, d_6): δ 170.6, 158.6, 155.9, 147.2, 146.6, 146.2, 145.7, 145.2, 145.2, 144.8, 144.5, 143.0, 142.5, 142.3, 142.0, 141.8, 139.9, 136.4, 136.2, 129.5, 128.5, 127.6, 127.16, 76.4, 71.2, 67.38, 62.44, 61.4, 60.2, 55.3, 53.3, 38.6, 26.0, 21.4, 21.2, 18.4, 17.1, 14.5. HPLC-MS (ESI): 12.44 min, [M+H$^+$] =1292.

Synthesis of 10. Compound **7** (170 mg, 0.33 mmol) was dissolved in dry CH$_3$CN (7 mL). Then HBTU (138 mg, 0.364 mmol) was added under nitrogen atmosphere. The mixture was stirred at room temperature for 10 minutes. A solution containing L-Val-OMe•HCl (55 mg, 0.33 mmol) and DIEA (0.185 mL, 1.09 mmol) in dry CH$_3$CN (3 mL) was then added dropwise, and the mixture was stirred for 5 h. The solvent was evaporated under vacuum. The residue was dissolved in CH$_2$Cl$_2$ and washed with distilled H$_2$O, 1M HCl, aqueous NaHCO$_3$ and H$_2$O. The organic layers were dried over Na$_2$SO$_4$, and the solvent was evaporated under vacuum. The crude residue was washed with Et$_2$O and *n*-hexane and filtered. Product **10** was obtained as a white solid with a yield of 90%.

M.p. 106-108 °C; IR (ATR-IR): ν 2979, 1784, 1747, 1733, 1717, 1701, 1681, 1672, 1653, 1557 cm^{-1}.^{1}H NMR (CDCl$_3$, 400 MHz): δ 0.92 (d, 6H, 2 CH$_3$-Val), 1.39 (d, 3H, CH$_3$-Oxd), 1.41 (9H, Boc), 1.49 (d, 3H, CH$_3$-Oxd), 1.51 (d, 3H, CH$_3$-Ala), 1.53 (d, 3H, CH$_3$-Ala) 2.15 (m, 1H, CHβ-Val), 3.70 (s, 3H, Val-OMe), 4.42 (d, 1H, CHα-Val), 4.46 (q, 2H, CHα-Ala), 4.69-4.81 (m, 2H, CHα-Oxd), 5.05 (d,1H, NH-Boc), 5.19-5.38 (m, 2H, CHβ-Oxd), 7.13 (d, 1H, NH amide), 7.34 (bs, 1H, NH amide). HPLC-MS (ESI): 8.08 min, [M+Na$^+$] = 650, [(M-Boc)+H$^+$] = 528.

Synthesis of 11. Product **10** (65.2 mg, 0.05 mmol) was dissolved in dry CH$_2$Cl$_2$ (2 mL), then TFA (18 equiv., 70 μL) was added, and the mixture was stirred for 4 h. When the deprotection was complete, the solvents were removed under reduced pressure and replaced with dry CH$_2$Cl$_2$ (2 mL). In another flask, 3-(tritylthio)propanoic acid (115 mg, 0.33 mmol) and HBTU (138 mg, 0.364 mmol) were dissolved in dry CH$_2$Cl$_2$ (6 mL) under nitrogen atmosphere. The mixture was stirred at room temperature for 10 minutes. The solution containing deprotected **8** and DIEA (*N,N*-diisopropylethylamine) (0.125 mL, 0.726 mmol) in dry CH$_2$Cl$_2$ (2 mL) was then added dropwise. The mixture was stirred for 5 h, then it was diluted with H$_2$O and extracted three times with CH$_2$Cl$_2$. The combined organic layers were dried over Na$_2$SO$_4$, and the solvent evaporated under vacuum. Product **12** was obtained as a yellowish solid after washing with Et$_2$O and *n*-hexane with a yield of 92%.

M.p. 158-160 °C. IR (ATR-IR): ν 3280, 3056, 2963, 2933, 1777, 1740, 1707, 1654, 1543 cm^{-1}. ^{1}H NMR (CDCl$_3$, 400 MHz): δ 0.91 (m, 6H, CH$_3$-Val), 1.31-1.40 (m, 6H, CH$_3$-Oxd), 1.46 (d, 3H, CH$_3$-Ala), 1.52 (d, 3H, CH$_3$-Ala), 1.93-2.24 (m, 3H, CHC*H*(CH$_3$)$_2$-Val, TrtSC*H$_2$*CH$_2$CO), 2.32-2.53 (m, 2H, SCH$_2$C*H$_2$*CO), 3.70 (s, 3H, OC*H$_3$*), 4.37-4.48 (m, 3H, CHα-Val, 2 CHα-Oxd), 4.59 (m, 1H, CHβ-Oxd), 4.76 (m, 1H, CHβ-Oxd), 5.24 (m, 2H, CHα-Ala), 6.26 (bs, 1H, NH), 7.15-7.43 (m, 15H, CH-Trt), 7.72 (bs, 1H, NH). HPLC-MS (ESI): 11.21 min, [M+Na$^+$] = 880.

Synthesis of 2. *S*-detritylation of **12** was obtained as reported in literature and previously described.[9] The residue was washed with *n*-hexane, and product **2** was obtained as a white solid in yield 75%.

M.p. 175-178 °C. IR (ATR-IR): ν 3273, 3065, 2963, 1779, 1739, 1706, 1652, 1537, 1447 cm^{-1}. ^{1}H NMR (CDCl$_3$, 400 MHz): δ 0.92 (m, 6H, CH$_3$-Val), 1.45-1.55 (m, 13H, CH$_3$-Ala, CH$_3$-Oxd, SH), 2.15 (m, 1H, CHC*H*(CH$_3$)$_2$-Val), 2.55 (m, 2H, HSC*H$_2$*CH$_2$CO), 2.75 (m, 2H, SCH$_2$C*H$_2$*CO), 3.71 (s, 3H, OC*H$_3$*), 4.42 (m, 1H, CHα-Val), 4.47 (m, 2H, CHα-Oxd), 4.68 (m, CHβ-Oxd), 4.79 (m, CHβ-Oxd), 5.36 (m, 2H, CHα-Ala), 7.12 (1H, NH), 7.39 (1H, NH), 7.63 (1H, NH). ^{13}C NMR (CDCl$_3$, 100 MHz): δ 173.6, 172.94, 171.9, 171.5, 167.5, 167.3, 151.8, 151.7, 75.2, 74.9, 62.7, 62.3, 58.1, 52.1, 49.1, 48.8, 39.5, 30.6, 21.4, 21.2, 20.1, 18.9, 18.6, 15.7. HPLC-MS (ESI): 6.77 min, [M+H$^+$] = 616, [M+Na$^+$] = 638.
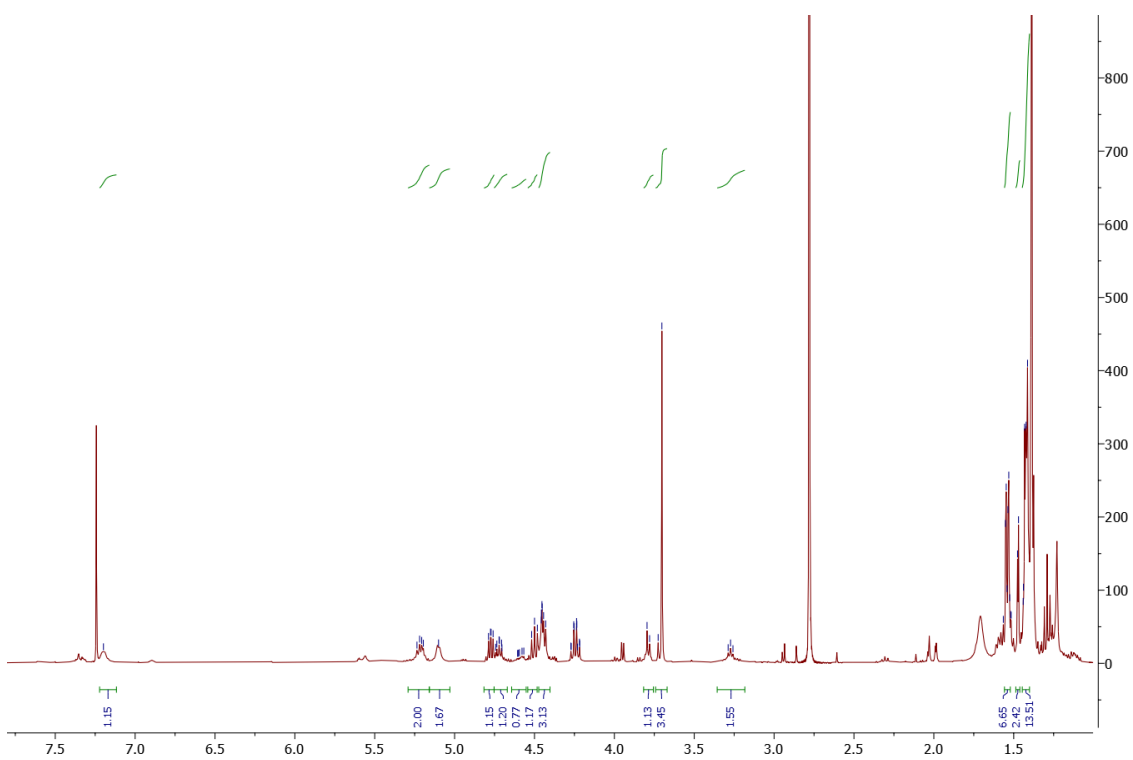
Figure S2. ^{1}H NMR spectrum of Product **8.**
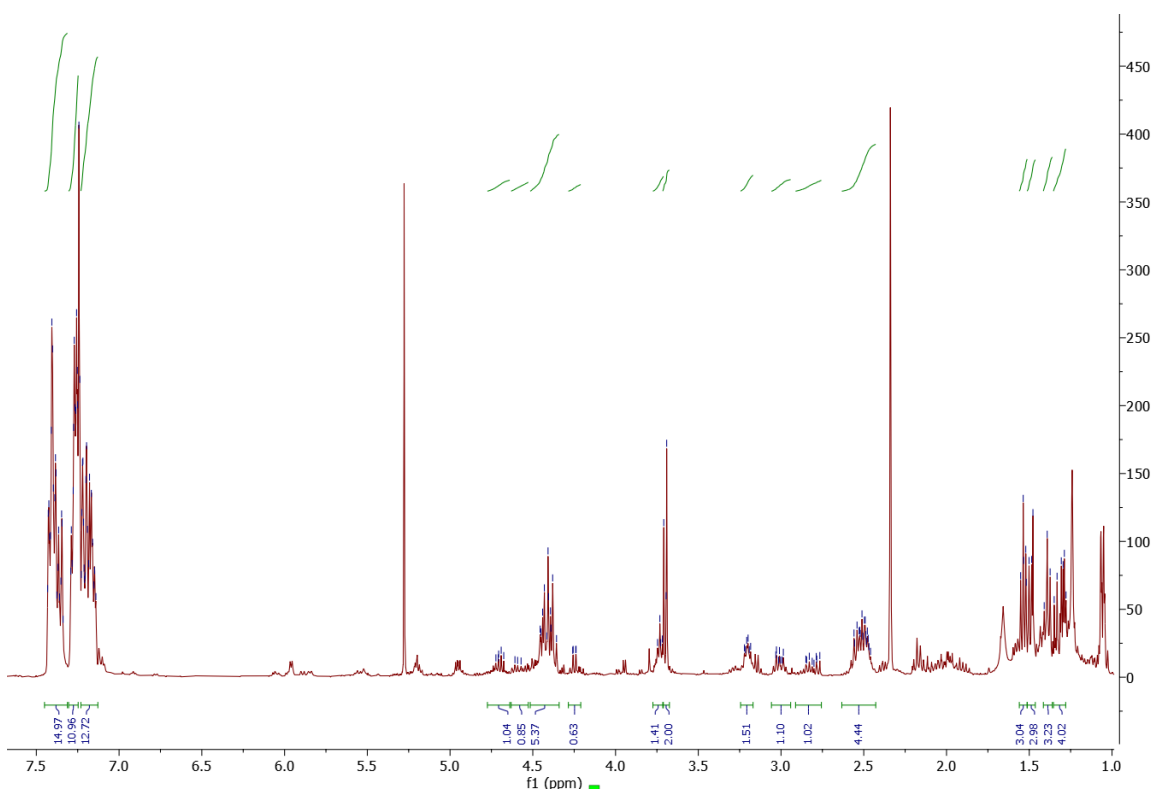

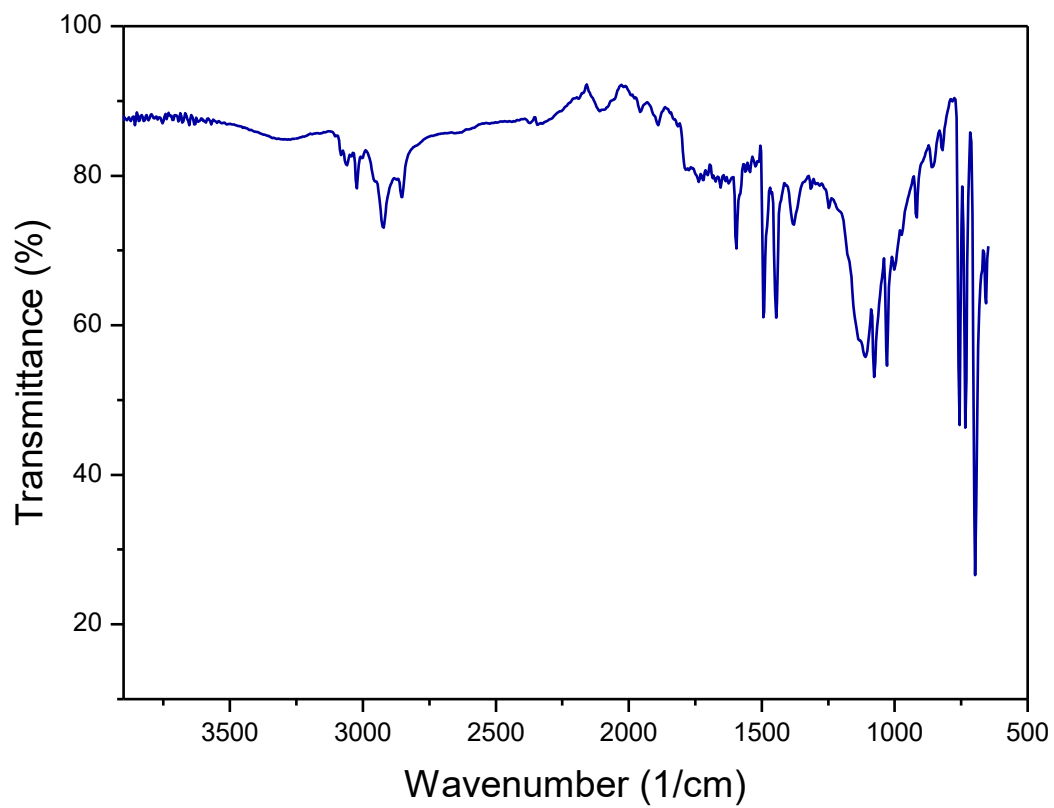**Figure S3.** ^{1}H NMR spectrum of Product **9.**

Figure S4. ATR-IR spectrum of product **1.**
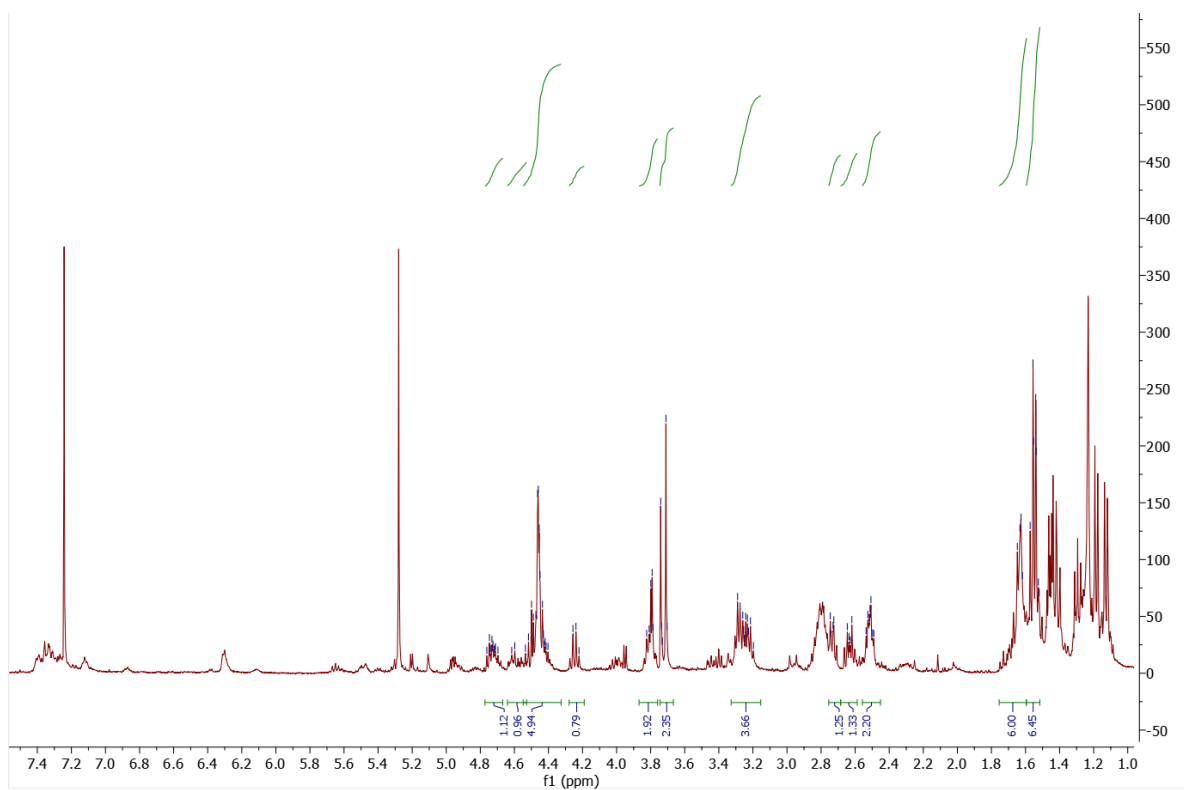
Figure S5. ^{1}H NMR spectrum of Product **1**
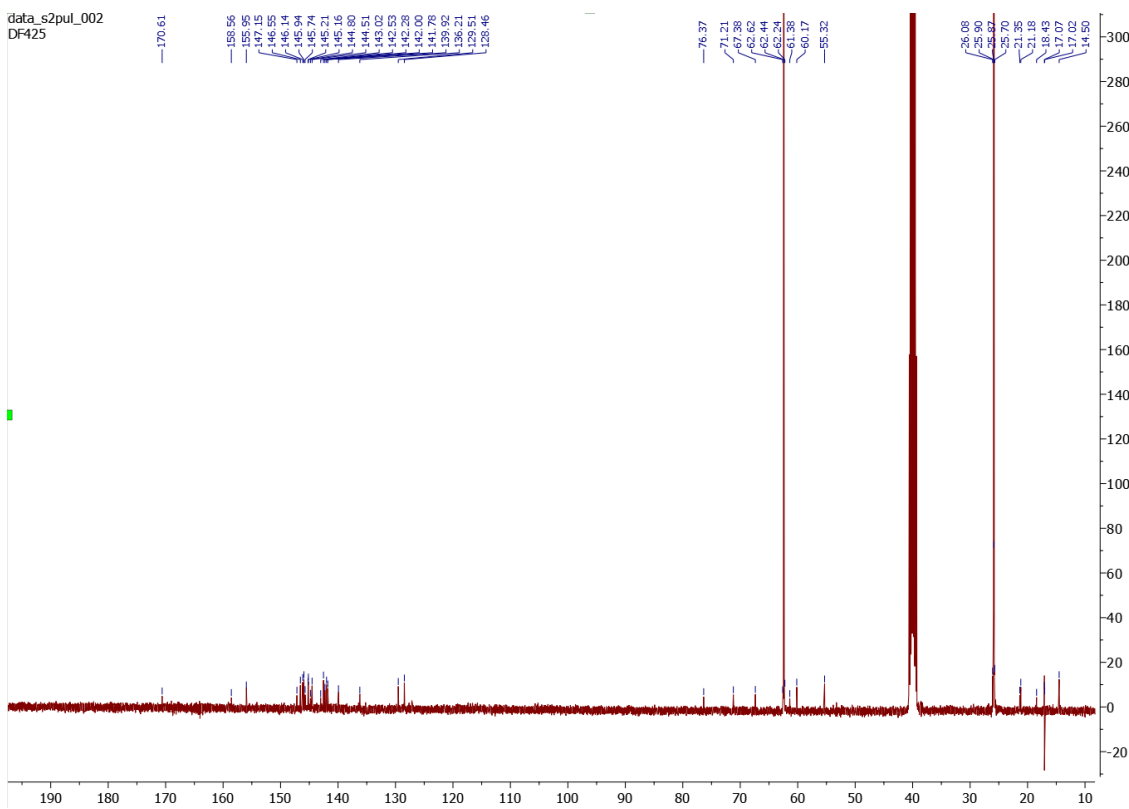
Figure S6. ^{13}C NMR spectrum of Product **1**.

E:\MS\DF522 F7 W2.D Injection 1 PDA - Total Absorbance Chromatogram

E:\MS\DF522_F7_W2.D Injection 1 Function 1 MS + spectrum 12.44
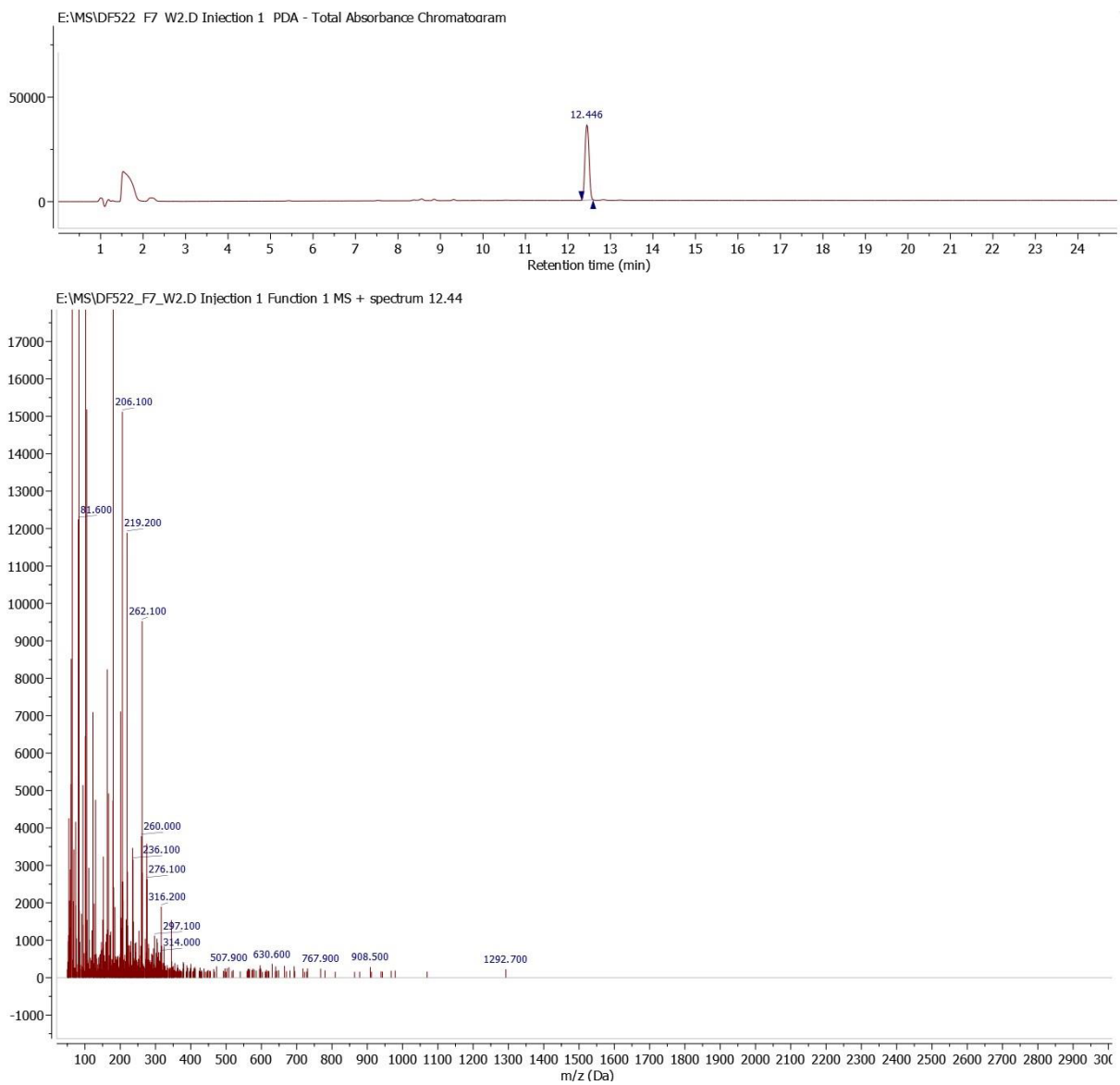
Figure S7. HPLC-MS analysis of product **1.**
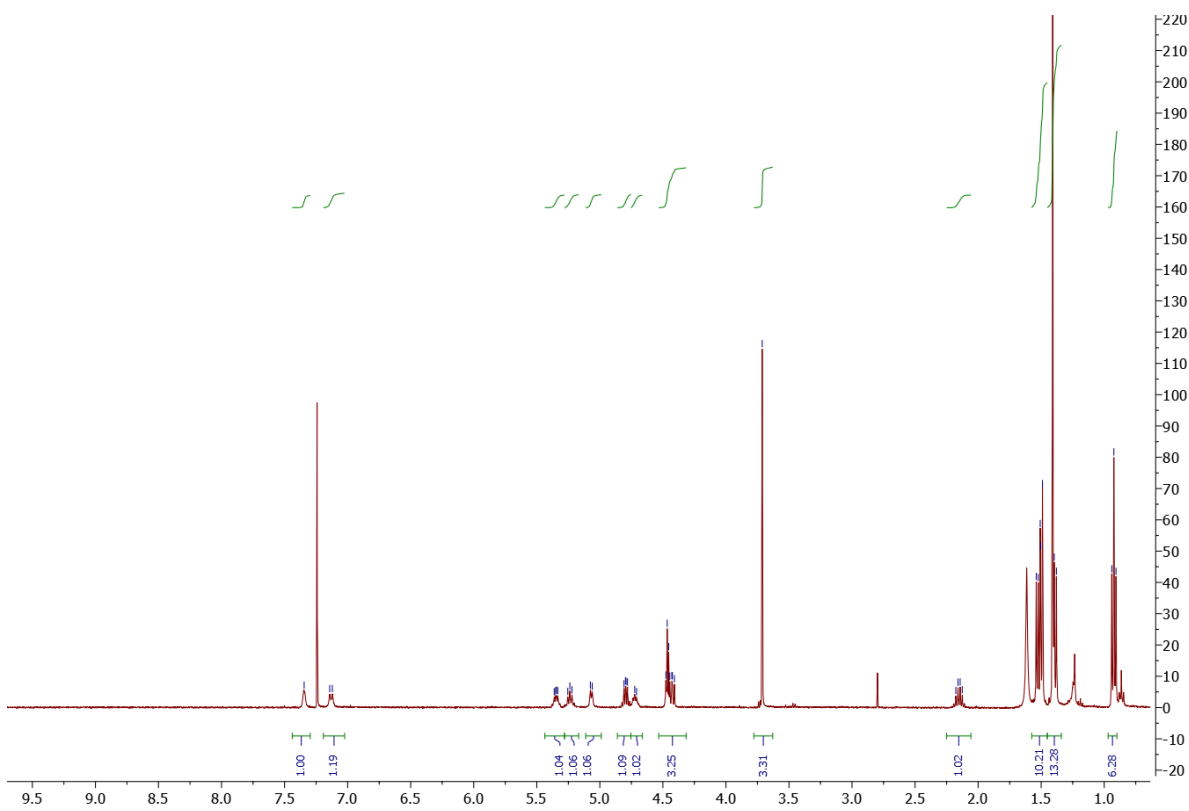
Figure S8. ^{1}H NMR spectrum of Product **10.**
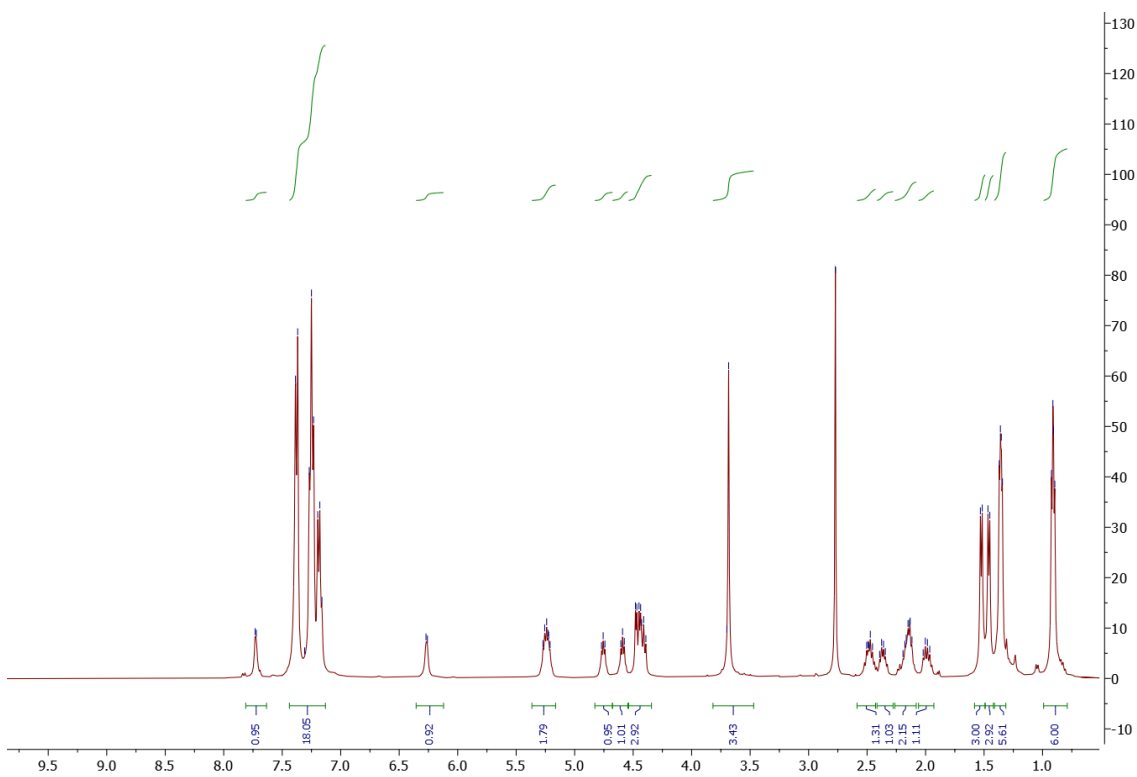

Figure S9. ^{1}H NMR spectrum of Product **11.**
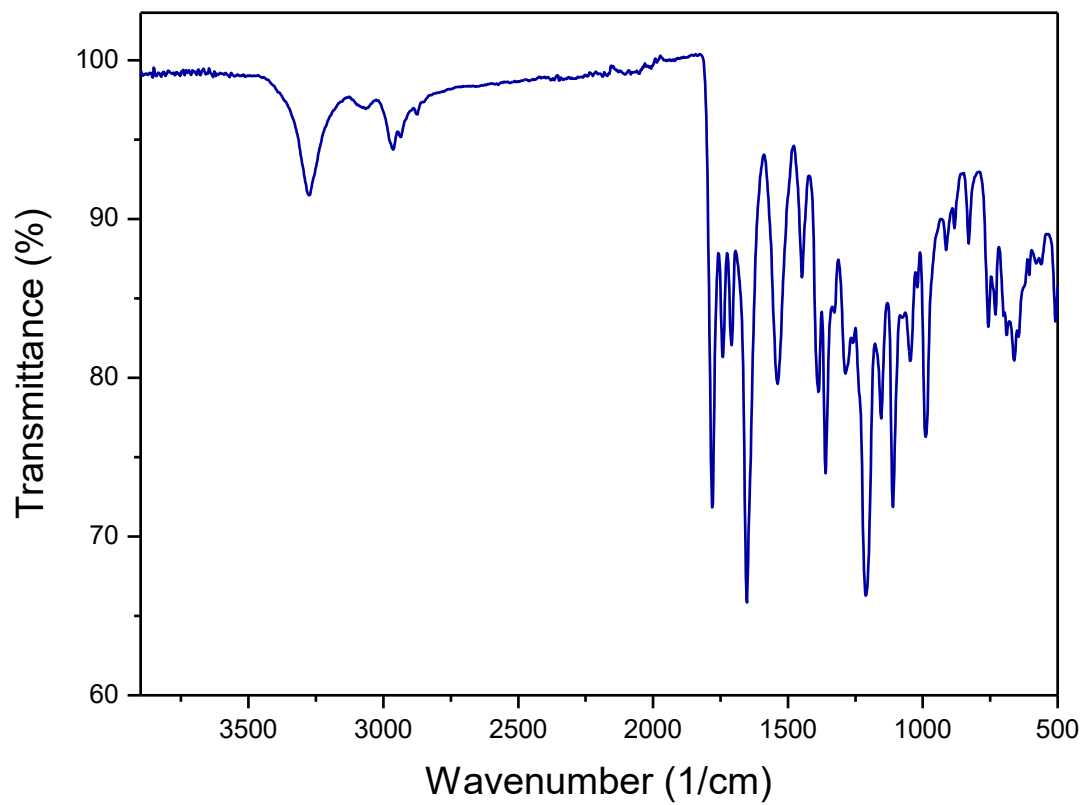
Figure S10. ATR-IR spectrum of product **2.**
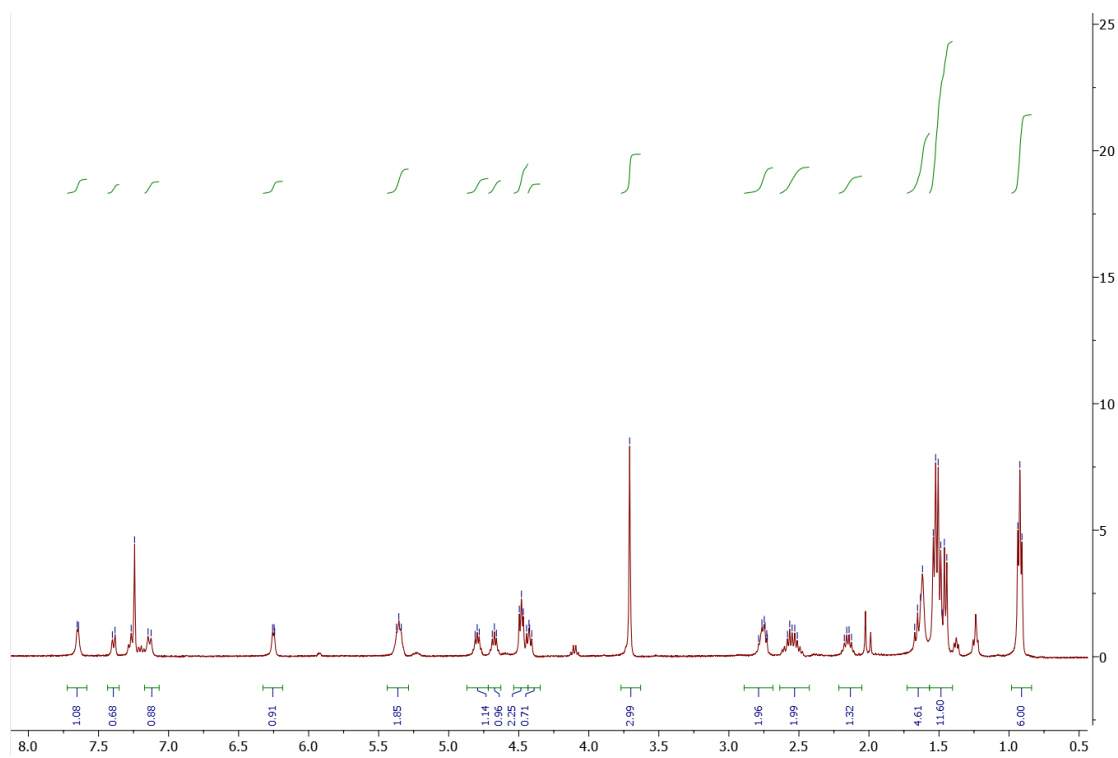
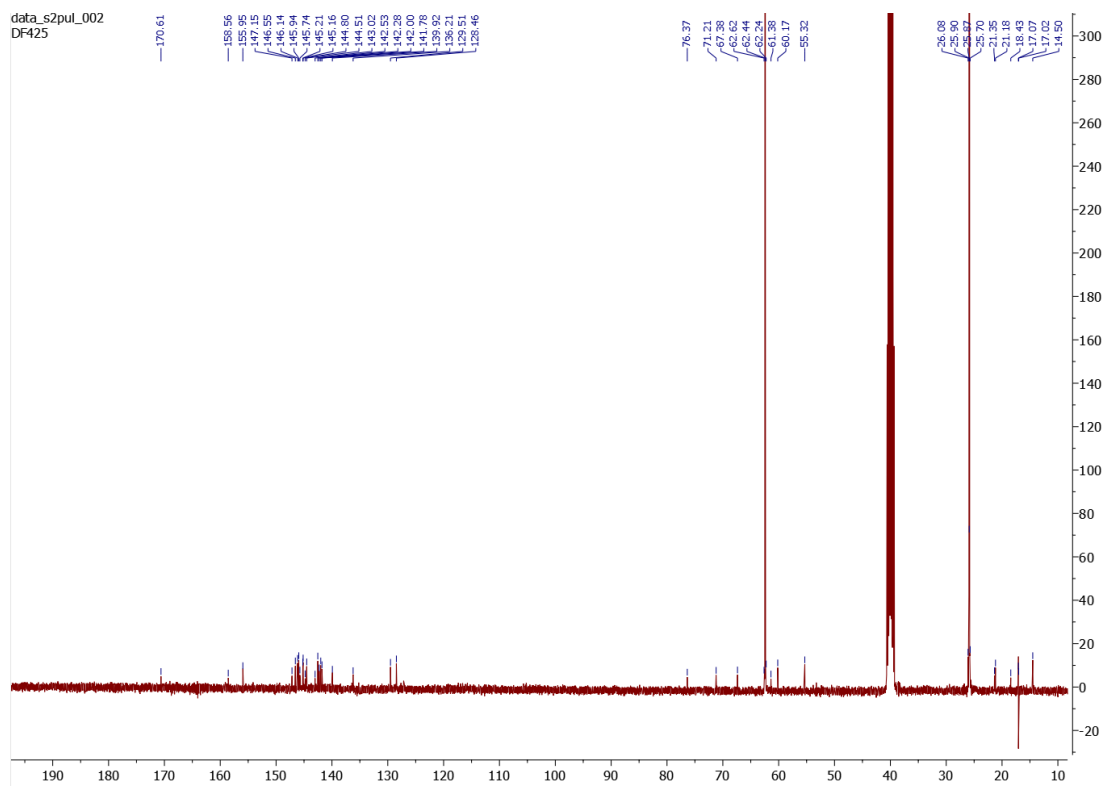**Figure S11.** ^{1}H NMR spectrum of Product **2.**

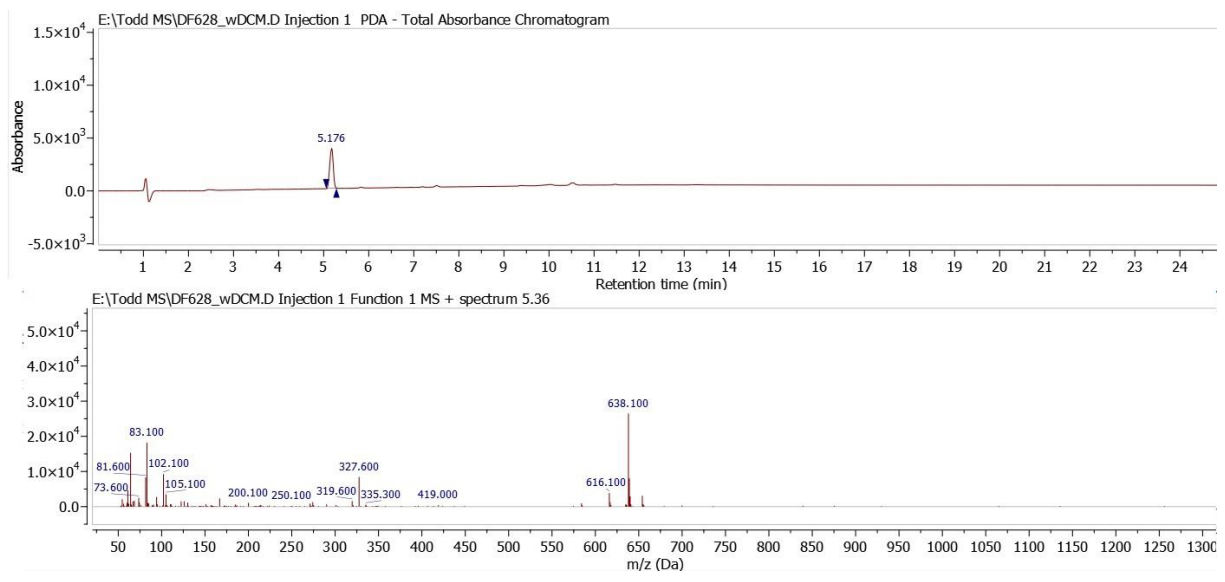**Figure S12.** ^{13}C NMR spectrum of Product **2.**

Figure S13. HPLC-MS analysis of product **2**

CdSe Quantum Dots (QDs) fabrication

Synthesis of pristine CdSe QDs

The CdSe QDs were prepared according to the hot injection method reported by Quanqin Dai *et al* with minor modifications.[10] Specifically, 0.473 mmol of CdO, 4.8 mmol of oleic acid, 14 mL of 1-octadecene, and 9.4 mmol of trioctyl phosphine oxide (TOPO) were loaded into a three-neck flask, and heated to 300°C under N_2 atmosphere. At this temperature, a TOP-Se solution (prepared by adding 1.7 mL of TOP to 0.93 mmol of Se powder in 4.1 mL of ODE) was swiftly injected. After the injection, the temperature was decreased to 270°C, and the CdSe QDs were let grow for 50 min. The reaction was quenched by removing the heating source and adding toluene. Finally, the CdSe QDs were purified by four washing steps centrifugating in ethanol at 4500 *g*, where *g* is the gravitational acceleration, and redispersing the precipitate in toluene, and finally dispersed in chloroform.

Morphological characterization

TOPO-capped QDs were characterized using Transmission Electron Microscopy (TEM) and Powder X-ray Diffraction (PXRD). TEM analysis was performed using a JEOL 100 SX, operating at 100 kV. Samples were prepared by drop casting a dilute suspension of CdSe QDs in hexane onto 200 mesh carbon-coated copper grids. The mean size and size distribution were obtained from statistical analysis over at least 300 CdSe QDs using the image J software.[11] Powder X-ray Diffraction (PXRD) measurements were carried out using a Bruker D8 Advance diffractometer equipped with a Cu Kα radiation and operating in Theta-Theta Bragg Brentano geometry at 40 kV and 40 mA.

TEM analysis reveals a size distribution of 5 nm with a standard deviation of 1 nm (Figure S1). PXRD measurements reveal broad diffraction peaks typical of QDs with similar size (Figure S2). The diffraction pattern is consistent with CdSe phases, while the reduced size of the crystallites makes difficult to univocally distinguish from cubic zinc blend or wurtzite crystal phases. This is typically reported for chalcogenide CdX (with X=S, Se, Te) QDs with size below 10 nm.[12]
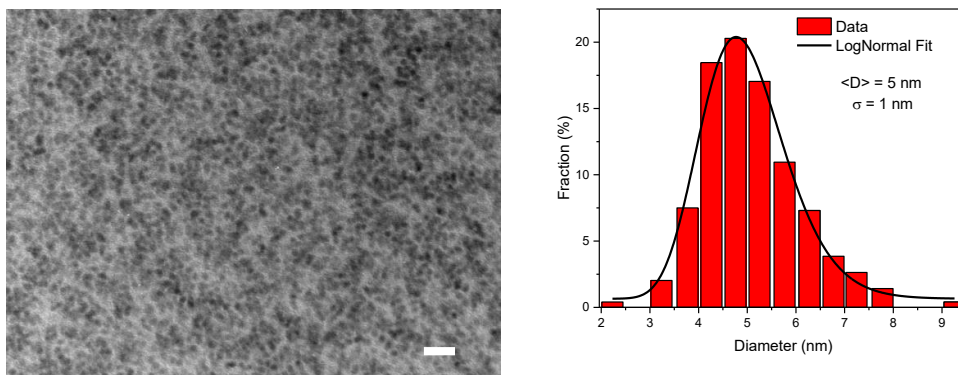
Figure S14: a) Representative TEM image of as-synthesized CdSe QDs (scale bar is 20 nm); b) size distribution obtained from statistical analysis of TEM images. The black line represents the fitting with a LogNormal distribution function. The average size <D> and standard deviation σ are displayed in the graph.

Figure S15: a) Diffraction pattern of as-synthesized CdSe QDs; b-c) reference pattern of the wurtzite (Powder Diffraction File: PDF 65-3415) and zinc blend (Powder Diffraction File: PDF 19-0191) CdSe crystal phases.

Ligand exchange

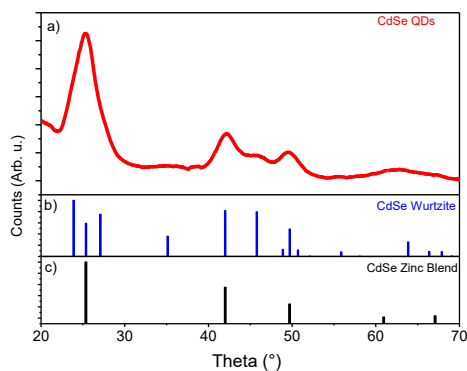8.5 mg of **1** were added to a solution containing 1.6 mg of TOPO-capped CdSe QDs in chloroform. The **1**-to-CdSe ratio was chosen considering a 10x molar excess with respect to the maximum number of molecules that can be adsorbed on the QDs surface considering a maximum packing density on the basis of the structure of the molecule. The mixture was kept under constant stirring overnight at room temperature. At the end of the ligand exchange process, the formed precipitate was observed and washed three times by centrifugation in ethanol. Absorption and luminescence spectra confirm the presence of the nanoparticles in the precipitate. Following a solubility test in different solvents (toluene, chloroform, dichloromethane, 1,2,4-trichlorobenzene), the **1**-capped QDs were finally dispersed in 1,2,4-trichlorobenzene.

A similar procedure was carried out to synthesise the control sample consisting of CdSe QDs ligand-exchanged with **2**.
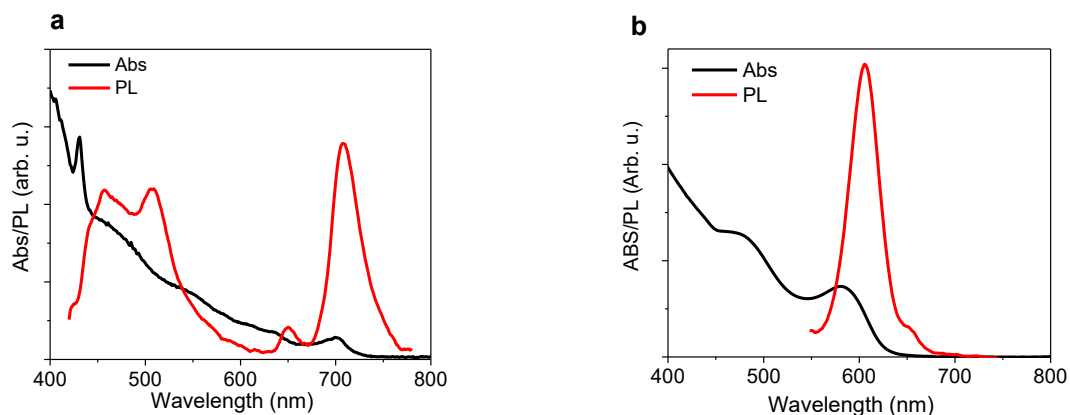
Optical spectroscopy

Figure S16: Absorption and photoluminescence spectra of (a) **1** and (b) the CdSe QDs functionalized with **2** (QDs-χ).
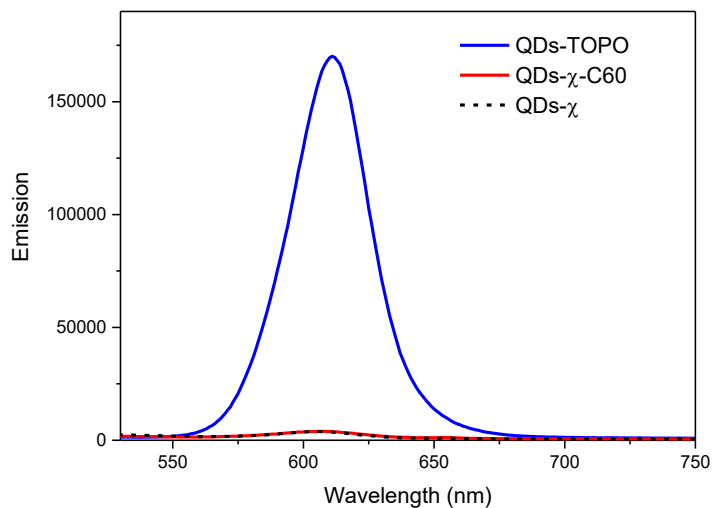
Figure S17: Comparison of the emission intensity of the CdSe QDs functionalized with TOPO (QDs-TOPO), **1 (**QDs-χ−C60) and **2** (QDs-χ) dispersed in 1,2,4-trichlorobenzene at the same concentration.
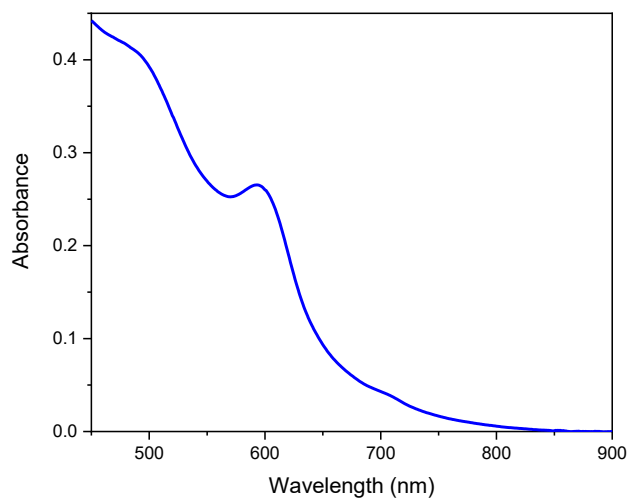
Figure S18: UV-vis absorption spectrum of the QD-χ-C60 solution used for EPR measurements normalized for the optical path. The absorbance is around 0.45 at 450 nm, which is approximately 5 times larger than the absorbance of the sample used for PL (reported in Figure 2a). No significant changes in the spectra at the two different concentrations are observed, the excitonic peak as well as a shoulder at 700 nm due to the C60 absorption are detected, thereby suggesting no aggregation of QDs is present in the studied concentration range.

	QD-χ-C60	CdSe QDs
τ_1 (a_1)	0.07 ns (0.99)	3.4 ns (0.65)
τ_2 (a_2)	2.1 ns (0.01)	18.0 ns (0.32)
τ_3 (a_3)	18.0 ns (0.0007)	81.4 ns (0.03)
$\langle \tau \rangle$	2.6 ns	29 ns

Table S1: Best fit values calculated from the triexponential fitting of TRPL curves in Figure 2b.

X-ray photoelectron spectroscopy (XPS)

XPS technique provided a chemical characterization of the functionalized CdSe QDs and confirmed the formation of a S-Cd bond between the **1** molecules and the CdSe QDs, as briefly described in the main text. The analysis of the Cd3d and Se3d regions (see Figures S22 and S23) confirms nanoparticles composition in line with what previously reported in the literature:[13] Cd3d spectra features a signal at 404.8 eV and its relative spin orbit, while in Se3d region a signal at 53.4 eV is present. In Figure 2c (main text), the C1s region spectra acquired on bulk molecules, on pristine CdSe QDs and on QD-χ-C60 system are reported. While in the spectrum of pure C_{60} only an intense signal at 285 eV arising from C=C species is found,[14] in the spectrum of **2** four components are needed to fit properly the experimental data, these components can be attributed to C-C (284.6 eV), C-N/C-O (286.5 eV), COOR (288.4 eV) and to a *shake-up* transition (290.3 eV).[15] The same components can be detected also in the spectrum of **1** with the exception of the one at lower binding energy which is covered by the presence of an intense component at 285.1 eV attributable to the C sp^2 belonging to the fullerene moiety of the molecules.[14] As a further reference, the C1s spectrum of CdSe QDs has been also collected; here, a main component at 284.3 eV is observed attributable to aliphatic carbon atoms of the TOPO ligand, plus a minor component at 285.8 eV attributable to adventitious carbon. Finally, the C1s region acquired on the QD-χ-C60 sample features all the components observed in previous systems suggesting the coexistence of both **1** and TOPO molecules after the exchange reaction. A decrease of the component attributable to TOPO has been observed and the low value of the ratio between the latter and the components belonging to the **1** molecules clarify that the residual TOPO contamination is a minority part of the system. A further confirmation of the presence of residual TOPO after the exchange with **1** is given by the observation of a P2p contribution at 132.4 eV[16] in the XPS spectra acquired on samples after the exchange reaction (see Figure S21).

A piece of crucial information regarding the correct assembly of molecules on the surface of nanoparticles can be deduced also by the analysis of S2p/Se3p region (Figure S20). In the spectra of

bulk molecules, a component attributable to thiol group at 163.5 eV and its relative spin orbit signal at higher binding energy (+1.18 eV) is observed.[17] In addition, a small component at ca. 167.1 eV is found and attributed to a partial oxidation of sulfur atoms of molecules.[18] In CdSe QDs sample a sulfur signal is not expected to be observed, while a Se3p signal (159.7 eV) and its relative spin orbit (+5.7 eV) are clearly visible.[13] In the QD-χ-C60 sample, due to the overlap of Se3p and S2p contribution, a change in the line shape of the spectra is observed which is given by the contemporary presence of selenium and an additional components at 161.8 eV attributable to sulfur atoms bound to the surface of the QDs.[19] This corroborates the correct assembly of molecules on the surface. Furthermore, the spectra do not feature a contribution at 163.5 eV as well as at ca. 167 eV excluding the presence of both physisorbed and oxidated molecules.

Figure S19: C 1s photoemission lines for the C$_{60}$, the **2** and **1** ligands, the CdSe QDs and the QD-χ-C$_{60}$ system, as well as the single chemically shifted components from fit deconvolution.

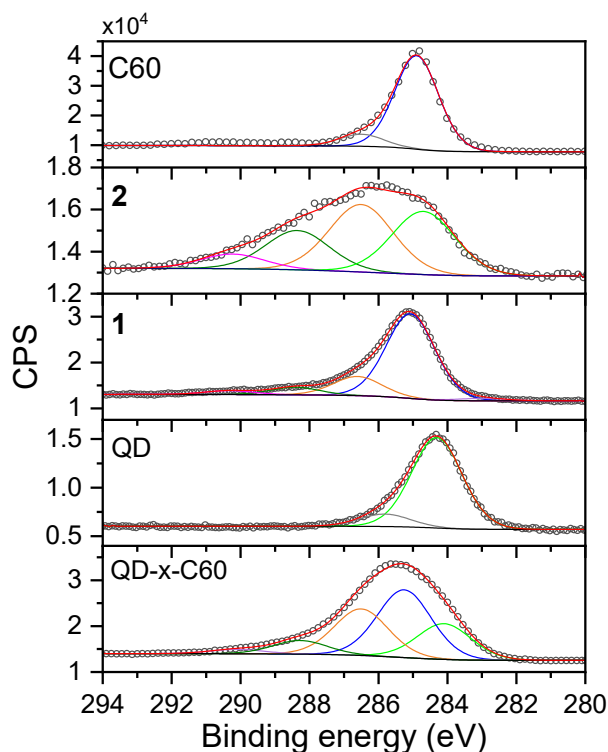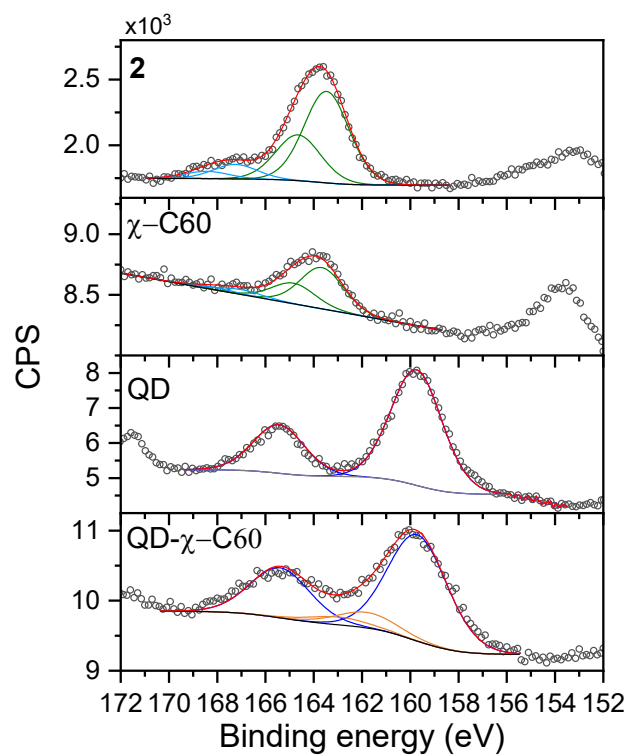**Figure S20:** S 2*p*/Se 3*p* photoemission lines for the **2** and **1** ligands, the CdSe QDs and the QD-χ-C$_{60}$ system, as well as the single chemically shifted components from fit deconvolution.

Figure S21: P 2*p* photoemission lines for the CdSe QDs and the QD-χ-C$_{60}$ system, as well as the single chemically shifted components from fit deconvolution.
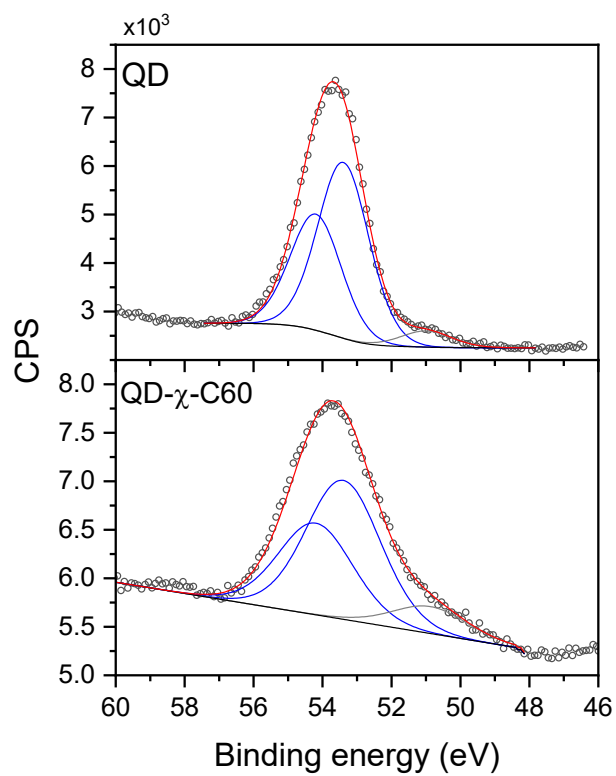
Figure S22: Se *3d* photoemission lines for the CdSe QDs and the QD-χ-C$_{60}$ system, as well as the single chemically shifted components from fit deconvolution.

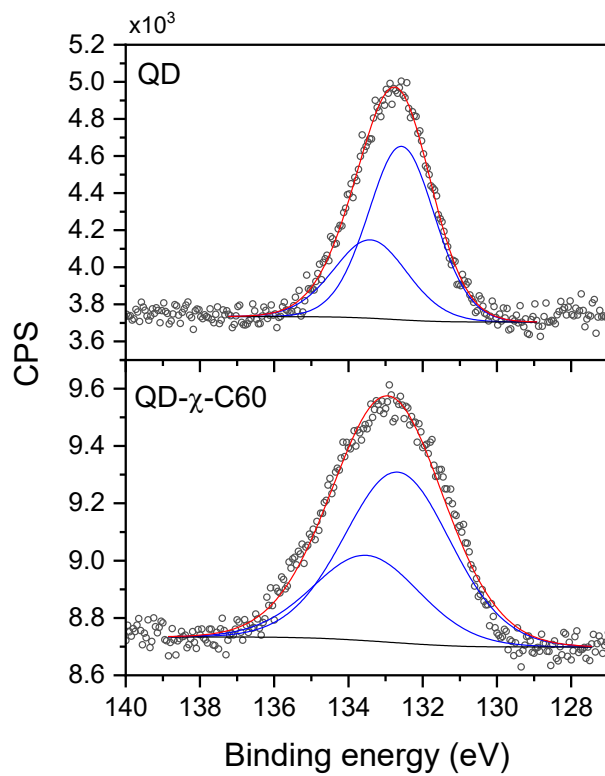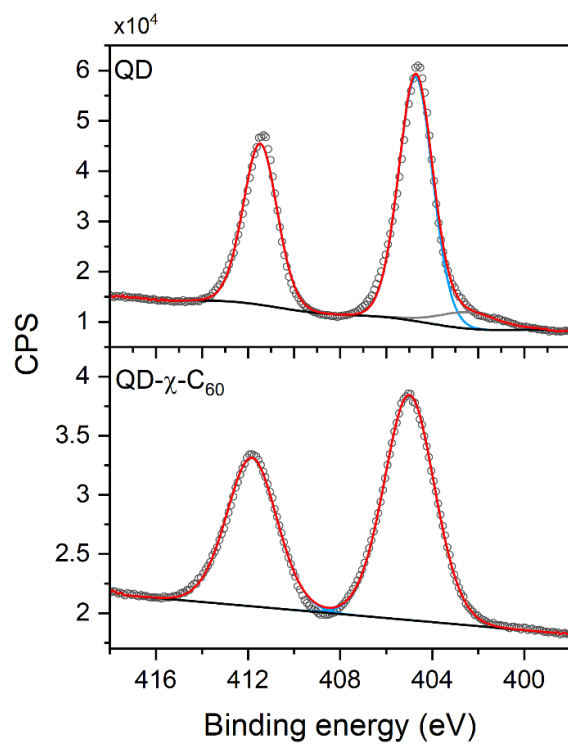**Figure S23:** Cd $3d$ photoemission lines for CdSe QDs and the QD-χ-C_{60} system, as well as the single chemically shifted components from fit deconvolution.

Time-resolved EPR

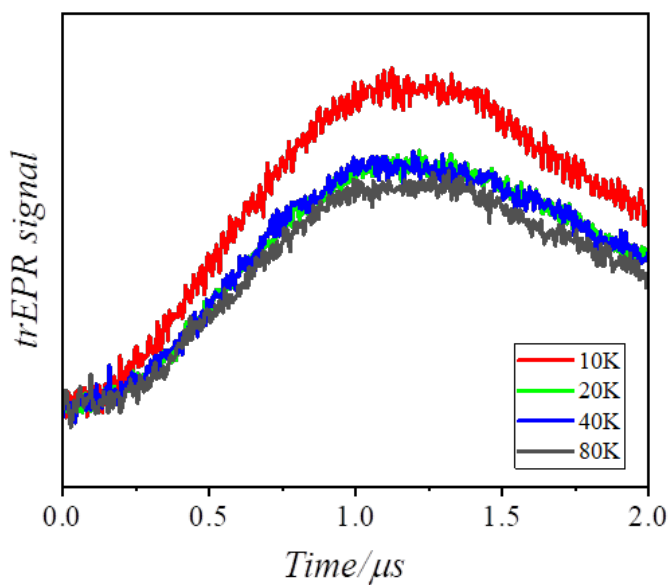**Figure S24:** trEPR transients of QD-χ-C60 excited at 450 nm in the temperature range T=10-80K. The transients are integrated on a magnetic field window of 0.5 mT and are centred at 346 mT. The transients at all temperatures show a maximum at around 1 µs after the laser pulse.

Theoretical modelling

General considerations

The spectra shown in the main text are all calculated through a spherical averaging over the three Euler angles $\{\theta, \phi, \chi\} \equiv \Omega$.

The fit of relaxation parameters was performed manually given the computational weight of the simulations, keeping the fitting parameters inside a physically reasonable range.

Simulation of incoherent time evolution

Spin relaxation, dephasing and charge recombination are introduced in our simulations through the super-operator L in the stochastic Liouville equation

$$\frac{\partial \rho}{\partial t} = -i[H, \rho] - L\rho$$

By defining $L = R + K$, we separate contributions from spin relaxation and dephasing (contained in the super-operator $R_{i,j,k,l}$), and charge recombination (in the super-operator $K_{i,j,k,l}$). The effect of the super-operators $R_{i,j,k,l}$ and $K_{i,j,k,l}$ is that of connecting the $\rho_{i,j}$ and the $\rho_{k,l}$ elements of the density matrix, where the indices (i, j, k, l) run over the four eigenstates of the Hamiltonian. Given the large difference between the two g-factors, the eigenstates are practically factorized, hence $i, j, k, l \in \{\uparrow\uparrow, \uparrow\downarrow, \downarrow\uparrow, \downarrow\downarrow\}$ (here, z is the direction of the external field). This allowed us to introduce two different spin relaxation times T_1^D and T_1^A, which are introduced in $R_{i,j,k,l}$ as:

$$R_{\uparrow\uparrow,\uparrow\uparrow,\uparrow\downarrow,\uparrow\downarrow} = \frac{1}{T_1^A \left(1 + e^{\frac{E_{\uparrow\uparrow} - E_{\uparrow\downarrow}}{k_B T}}\right)} \, , R_{\uparrow\downarrow,\uparrow\downarrow,\uparrow\uparrow,\uparrow\uparrow} = R_{\uparrow\uparrow,\uparrow\uparrow,\uparrow\downarrow,\uparrow\downarrow} e^{\frac{E_{\uparrow\uparrow} - E_{\uparrow\downarrow}}{k_B T}}$$

$$R_{\uparrow\uparrow,\uparrow\uparrow,\downarrow\uparrow,\downarrow\uparrow} = \frac{1}{T_1^D \left(1 + e^{\frac{E_{\uparrow\uparrow} - E_{\downarrow\uparrow}}{k_B T}}\right)} \, , R_{\downarrow\uparrow,\downarrow\uparrow,\uparrow\uparrow,\uparrow\uparrow} = R_{\uparrow\uparrow,\uparrow\uparrow,\downarrow\uparrow,\downarrow\uparrow} e^{\frac{E_{\uparrow\uparrow} - E_{\downarrow\uparrow}}{k_B T}}$$

$$R_{\uparrow\downarrow,\uparrow\downarrow,\downarrow\downarrow,\downarrow\downarrow} = \frac{1}{T_1^D \left(1 + e^{\frac{E_{\uparrow\downarrow} - E_{\downarrow\downarrow}}{k_B T}}\right)} \, , R_{\downarrow\downarrow,\downarrow\downarrow,\uparrow\downarrow,\uparrow\downarrow} = R_{\uparrow\downarrow,\uparrow\downarrow,\downarrow\downarrow,\downarrow\downarrow} e^{\frac{E_{\uparrow\downarrow} - E_{\downarrow\downarrow}}{k_B T}}$$

$$R_{\downarrow\uparrow,\downarrow\uparrow,\downarrow\downarrow,\downarrow\downarrow} = \frac{1}{T_1^A \left(1 + e^{\frac{E_{\downarrow\uparrow}-E_{\downarrow\downarrow}}{k_B T}} \right)} \quad , R_{\downarrow\downarrow,\downarrow\downarrow,\downarrow\uparrow,\downarrow\uparrow} = R_{\downarrow\uparrow,\downarrow\uparrow,\downarrow\downarrow,\downarrow\downarrow} \, e^{\frac{E_{\downarrow\uparrow}-E_{\downarrow\downarrow}}{k_B T}}$$

We also introduced the relaxation terms between $\downarrow\uparrow$ and $\uparrow\downarrow$, which are defined based on a third relaxation time T_{bc}. For simplicity, in our simulations we assumed $T_{bc} = T_1^D$. The remaining diagonal elements of $\boldsymbol{R}$ are given by the stationary condition $\sum_j R_{jjii} = 0$.

Spin dephasing is also contained in the super-operator $\boldsymbol{R}$ and is defined as:

$$R_{i,j,i,j} = -\frac{1}{T_2} \, , i \neq j$$

Charge recombination was instead accounted for in $K_{i,j,k,l}$, defined on the singlet-triplet basis $i, j, k, l \in \{S, T_-, T_0, T_+\}$. The elements of $K_{i,j,k,l}$ are determined as:

$$K_{i,j,k,l} = K'_{i,k}\delta_{j,l} + K'_{j,l}\delta_{i,k} \, , K'_{i,j} = -\frac{1}{2}(k_S Q_S + k_T Q_T)_{i,j}$$

Where k_S and k_T are the charge recombination rates from the singlet state and from the triplet states, respectively; Q_S and Q_T are projectors onto the subspaces defined by the same states.
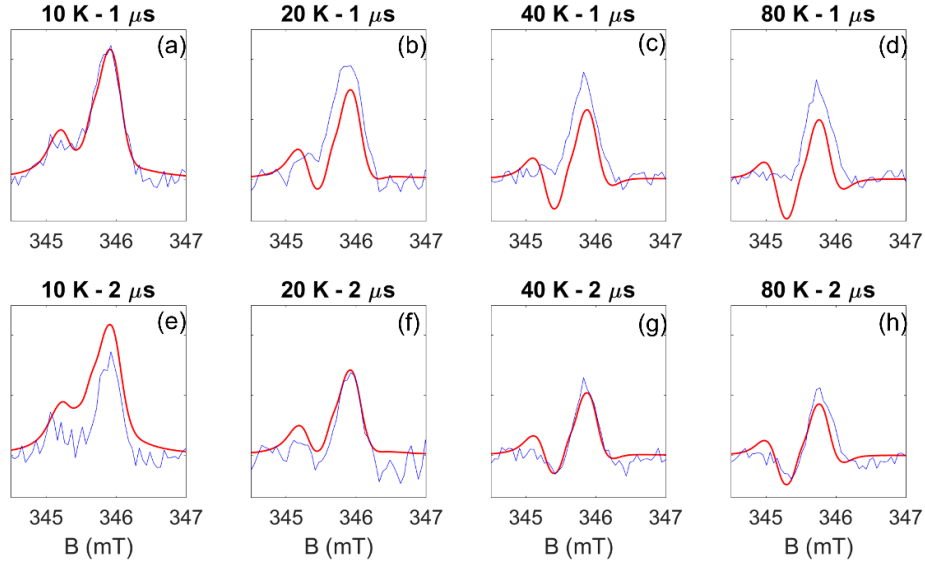
Comparing experiment and simulation

Figure S25: Comparison of experiments and simulations at t=1, 2μs and at T=10, 20, 40, 80K. All simulations were performed using the parameters in Table T1 of the main text and with the ST initial state in the absence of CISS effect.

CISS initial state

The effect of CISS is included in our simulations as a "filter" applied on the initial state $\rho(0)$. This is achieved using the following projector, written on the $\{\uparrow\uparrow, \uparrow\downarrow, \downarrow\uparrow, \downarrow\downarrow\}$ local molecular basis:

$$P_{CISS} = \begin{pmatrix} 1 & 0 & 0 & 0 \\ 0 & 0 & 0 & 0 \\ 0 & 0 & 1 & 0 \\ 0 & 0 & 0 & 0 \end{pmatrix}$$

Which is used to generate the initial CISS state as $\rho_{CISS}(0) = P_{CISS}\, \rho(0)\, P_{CISS}$. Here, the transferred electron spin on the C_{60} anion is forced to be in the $\uparrow$ orientation, whereas the spin on the QD retains its initial superposition.

Anisotropic initial state

To further validate our conclusions, we probed different initial states with respect to those reported in the main text. Specifically, we explored those cases that do not possess spherical symmetry. To do

this, we need to perform an additional spherical average over the solid angle Ω' between the initial state and the chiral bridge (performed in the same fashion of the one over Ω introduced above). This average reflects the approximately spherical distribution of chiral bridges on the QD surface.

The case in which the CISS filter is not implemented in the calculations is straightforward: the additional spherical average can be performed on $\rho(0)$ alone, leading to an equal mixing of the triplet sublevels, regardless of their initial differences in populations. Obviously, such average cannot mix singlet and triplet energy levels, whose relative populations determine the shape of the spectra just like it was shown in the main text.

Conversely, when implementing the CISS filter, the initial state depends on the angles of both spherical averages, which cannot be performed independently. We carried out enough simulations to determine the effect of different population distributions between singlet and triplet states. An example is reported in Fig. S23.

Even in presence of CISS filter, we found that the relative populations of the three triplet states do not have a significant effect on the shape of the spectra. Even in this case, the most relevant aspect of the initial state when fitting experimental data was the relative population between the triplet and the singlet states. If the S population approaches $\approx 1/4$ the short-time signal disappears, independently of the specific populations of the T_+, T_0 and T_- levels.

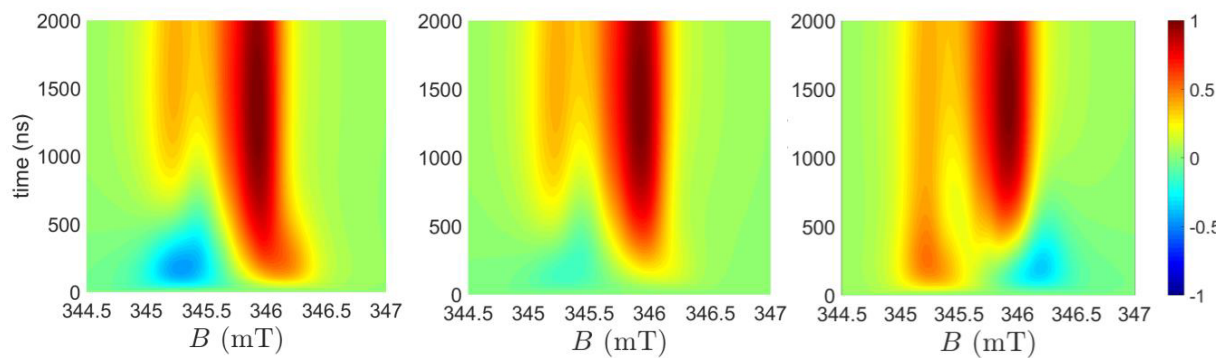**Figure S26:** Results of simulations with two spherical averages for two different initial states. In the left panel the initial population of the different states is: $S = 0.4$, $T_+ = 0.05$, $T_0 = 0.35$ and $T_- = 0.2$. In the central panel the populations are $S = 0.25$, $T_+ = 0.05$, $T_0 = 0.20$ and $T_- = 0.50$. In the right panel the populations are $S = 0.1$, $T_+ = 0.2$, $T_0 = 0.3$ and $T_- = 0.4$.

Bibliography

1. Neese, F., Software update: the ORCA program system, version 4.0. *WIREs Comput. Mol. Sci.* **2018,** *8*, e1327.

2. Adamo, C.; Barone, V., Toward reliable density functional methods without adjustable parameters: The PBE0 model. *J. Chem. Phys.* **1999,** *110*, 6158-6170.

3. Grimme, S.; Ehrlich, S.; Goerigk, L., Effect of the damping function in dispersion corrected density functional theory. *J. Comput. Chem.* **2011,** *32*, 1456-1465.

4. Grimme, S.; Antony, J.; Ehrlich, S.; Krieg, H., A consistent and accurate ab initio parametrization of density functional dispersion correction (DFT-D) for the 94 elements H-Pu. *J. Chem. Phys.* **2010,** *132*, 154104.

5. Weigend, F.; Ahlrichs, R., Balanced basis sets of split valence, triple zeta valence and quadruple zeta valence quality for H to Rn: Design and assessment of accuracy. *Phys. Chem. Chem. Phys.* **2005,** *7*, 3297-3305.

6. Muller, D.; Zeltser, I.; Bitan, G.; Gilon, C., Building Units for N-Backbone Cyclic Peptides. 3. Synthesis of Protected Nα-(ω-Aminoalkyl)amino Acids and Nα-(ω-Carboxyalkyl)amino Acids. *J. Org. Chem.* **1997,** *62*, 411-416.

7. Kordatos, K.; Da Ros, T.; Bosi, S.; Vázquez, E.; Bergamin, M.; Cusan, C.; Pellarini, F.; Tomberli, V.; Baiti, B.; Pantarotto, D.; Georgakilas, V.; Spalluto, G.; Prato, M., Novel Versatile Fullerene Synthons. *J. Org. Chem.* **2001,** *66*, 4915-4920.

8. Tomasini, C.; Luppi, G.; Monari, M., Oxazolidin-2-one-Containing Pseudopeptides That Fold into β-Bend Ribbon Spirals. *J. Am. Chem. Soc.* **2006,** *128*, 2410-2420.

9. Kicsák, M.; Bege, M.; Bereczki, I.; Csávás, M.; Herczeg, M.; Kupihár, Z.; Kovács, L.; Borbás, A.; Herczegh, P., A three-component reagent system for rapid and mild removal of O-, N- and S-trityl protecting groups. *Org. Biomol. Chem.* **2016,** *14*, 3190-3192.

10. Dai, Q.; Li, D.; Chen, H.; Kan, S.; Li, H.; Gao, S.; Hou, Y.; Liu, B.; Zou, G., Colloidal CdSe Nanocrystals Synthesized in Noncoordinating Solvents with the Addition of a Secondary Ligand: Exceptional Growth Kinetics. *J. Phys. Chem. B* **2006,** *110*, 16508-16513.

11. Schneider, C. A.; Rasband, W. S.; Eliceiri, K. W., NIH Image to ImageJ: 25 years of image analysis. *Nat. Methods* **2012,** *9*, 671-675.

12. Holder, C. F.; Schaak, R. E., Tutorial on Powder X-ray Diffraction for Characterizing Nanoscale Materials. *ACS Nano* **2019,** *13*, 7359-7365.

13. Ospina, R.; Rincón-Ortiz, S. A.; Rodriguez-Pereira, J., Cadmium selenide by XPS. *Surf. Sci. Spectra* **2020,** *27*, 014021.

14.   Vasquez, R. P.; Brain, R. A.; Ross, D.; Yeh, N.-C., Epitaxial C60 Film on Si(111) by XPS. *Surf. Sci. Spectra* **1992,** *1*, 242-245.

15.   Chen, X.; Wang, X.; Fang, D., A review on C1s XPS-spectra for some kinds of carbon materials. *Fullerenes, Nanotubes and Carbon Nanostructures* **2020,** *28*, 1048-1058.

16.   Morris-Cohen, A. J.; Donakowski, M. D.; Knowles, K. E.; Weiss, E. A., The Effect of a Common Purification Procedure on the Chemical Composition of the Surfaces of CdSe Quantum Dots Synthesized with Trioctylphosphine Oxide. *J. Phys. Chem. C* **2010,** *114*, 897-906.

17.   Lau, K. H. A.; Huang, C.; Yakovlev, N.; Chen, Z. K.; O'Shea, S. J., Direct Adsorption and Monolayer Self-Assembly of Acetyl-Protected Dithiols. *Langmuir* **2006,** *22*, 2968-2971.

18.   Volmer, M.; Stratmann, M.; Viefhaus, H., Electrochemical and electron spectroscopic investigations of iron surfaces modified with thiols. *Surf. Interface Anal.* **1990,** *16*, 278-282.

19.   Liu, S.; Zhang, X.; Yu, Y.; Zou, G., Bandgap engineered and high monochromatic electrochemiluminescence from dual-stabilizers-capped CdSe nanocrystals with practical application potential. *Biosens. Bioelectron.* **2014,** *55*, 203-208.

20.   Righetto, M.; Privitera, A.; Carraro, F.; Bolzonello, L.; Ferrante, C.; Franco, L.; Bozio, R., Engineering interactions in QDs-PCBM blends: a surface chemistry approach. *Nanoscale* **2018,** *10*, 11913-11922.

21.   Ramirez, I.; Privitera, A.; Karuthedath, S.; Jungbluth, A.; Benduhn, J.; Sperlich, A.; Spoltore, D.; Vandewal, K.; Laquai, F.; Riede, M., The role of spin in the degradation of organic photovoltaics. *Nat. Commun.* **2021,** *12*, 471.